Survey of Optical Environment over Hemisphere-on-Cylinder Turret Using Suite of Wavefront Sensors

Stanislav Gordeyev[*]
University of Notre Dame, Notre Dame, IN, 46556

Martiqua L. Post[†],
U.S. Air Force Academy, USAF Academy, CO

Thomas McLaughlin[‡],
U.S. Air Force Academy, USAF Academy, CO

Juan Ceniceros[§],
The Boeing Company, Albuquerque, NM

and

Eric J. Jumper[**]
University of Notre Dame, Notre Dame, IN, 46556

Extensive measurements of the optical environment around a generic hemisphere-on-cylinder turret with a conformal window were performed for both forward- and backward-looking elevation angles using a Malley probe, conventional 2-D wavefront sensor and high-bandwidth 8x8 wavefront sensor for a range of Mach numbers from 0.35 to 0.45. A necklace vortex at the bottom of the turret and the shear layer structures formed in the separated region of the flow were identified as the main causes of optical distortions imposed on a laser beam. Different instruments provide different, but complimentary information about the aberrating structures. The Malley probe data can distinguish between stationary and traveling aberrations, but provides 1-D slices of wavefronts only, while the 2-D wavefront sensor data gives time-uncorrelated sets of highly spatially resolved wavefronts. The high-bandwidth, 8x8 wavefront sensor data provides a unique opportunity to decompose wavefronts into their stationary and convective components. Oil-flow visualization revealed a complex topology of the flow around the turret.

I.   Introduction

Turrets provide a convenient way of propagating an airborne laser beam from an airborne platform. But its non-optimal aerodynamic shape creates elevated levels of turbulent fluctuations around the turret, which in turn impose optical distortions on the emanating laser beam[1,2].

In general, the subsonic flow around a generic turret is quite complex as is depicted schematically in Figure 1. The incoming boundary is wrapped around the turret forming a necklace vortex. Flow stays attached on the upstream portion of the turret and separates on the downstream portion. The separation line is Reynolds number dependent. After the flow separates behind the turret, shear layer structures form shortly downstream of the separated point. These structures interact with the wake region and the necklace vortex downstream of the turret and create high levels of turbulence[3]. These turbulent vortical structures impose significant distortions on the laser beam, thus typically restricting viewing angles to a forward quadrant of the turret[4].

---

[*] Research Assistant Professor, Department of Aerospace and Mech. Eng., University of Notre Dame, IN, Member AIAA.
[†] Position, Department of Aeronautics, USAF Academy, CO, Member AIAA
[‡] Director of Research, Department of Aeronautics, USAF Academy, CO, Assoc. Fellow AIAA
[§] Program Manager, JTO Aero-Optics, Boeing-SVS, Inc., AIAA Affiliation.
[**] Professor, Department of Aerospace and Mech. Eng., University of Notre Dame, IN, Fellow AIAA.

Optical aberrations around a turret with a flat window were extensively investigated in Ref 5. A slope discontinuity between the turret and the flat window forces the flow to separate prematurely, at elevation angles around 100 degrees. Shear layer structures formed in the separation region of the flow were shown to be a main reason for high optical distortions for backward-looking angles; the use of passive devices placed upstream of the flat window was shown to be effective in disrupting and/or delaying the shear layer structure formation and consequently extended the viewing angles up to 120 degrees[6].
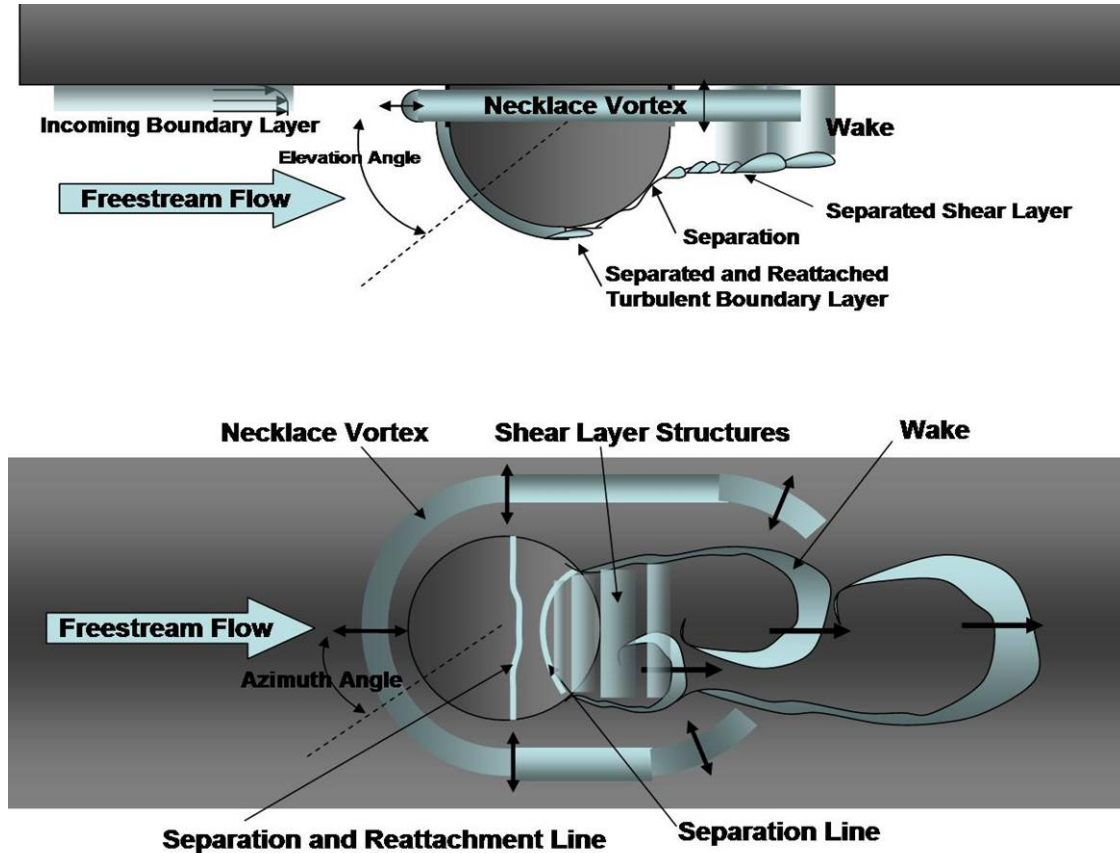

Figure 1. Flow topology around the conformal-window turret.

One way to avoid a premature shear layer formation is to use a conformal window turret where a leading radius of the optical component matches the turret's radius. This geometry is the focus of the present work. The optical environment was extensively studied at different elevation angles and subsonic Mach numbers using three different sensors for measuring optical wavefronts: (i) a Malley probe, (ii) a commercially-available 2-D wavefront sensor and (iii) a high-bandwidth 8x8 wavefront sensor, capable of sampling wavefronts continuously with sampling rates up to and exceeding 100 kHz, although the sampling rate for the present work was 78 kHz. These measurements were complimented by steady and unsteady pressure measurements on the turret and in the wake, as well as an oil-based visualization of the surface-flow topology on and around the turret.

II.   Experimental Set-Up

All experiments were conducted in the Subsonic Wind Tunnel at the Air Force Academy, Colorado Springs, Colorado. This tunnel has 3ft x 3ft x 8 ft test section and is capable of achieving Mach numbers up to 0.6, although run times at high Mach numbers above 0.45 are relatively short due to tunnel heating. In the present study test Mach numbers were chosen to be 0.35, 0.4 and 0.45.

Wind tunnel tests were conducted on the conformal-window hemisphere-on-cylinder "turret" model shown mounted on the back wall of the Academy tunnel in Figure 2, left. A cross-sectional dimensional drawing is presented in Figure 2, right; all dimensions are in inches. The turret was placed on the back side of the test section 54" downstream from the beginning of the test section. The 12" diameter turret is composed of a sphere mated to a

cylindrical base of 4.5" height. The hollow sphere is made of plastic and re-enforced by adding epoxy material to create a thicker wall. The sphere is fitted with a flush-mounted, positive lens with an outer radius of curvature that matches the 6" curvature of the sphere. Details of the optical components will be discussed later. The sphere can be rotated along a vertical axis, as in an overhead pass, thus allowing any elevation angle between 40 and 140 degrees. The cylinder was mounted on a flat plate and could be rotated to any azimuth angle. The open cylinder's end was sealed with a flat aluminum plate, so that the interior of the turret was nominally at the test-section static pressure.
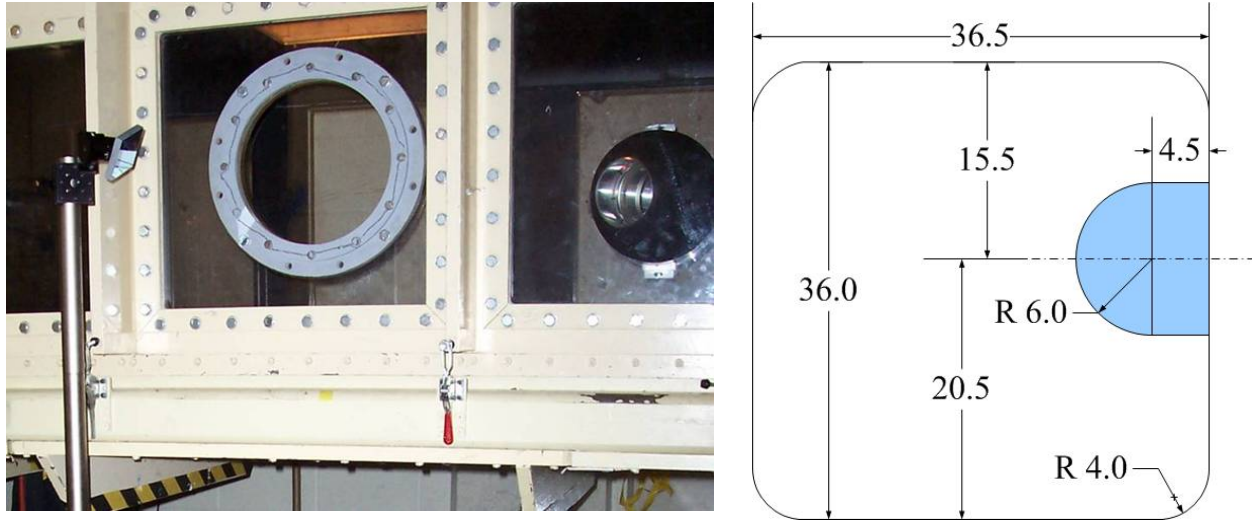
Figure 2. Left: Turret is mounted on the back side of the tunnel. Right: Dimensional drawing of the tunnel's cross-section with the mounted turret.

The turret was equipped with 10 static pressure ports and 3 Kulite unsteady pressure sensors; 1 mounted on the turret and 2 mounted on the mounting plate downstream of the turret.
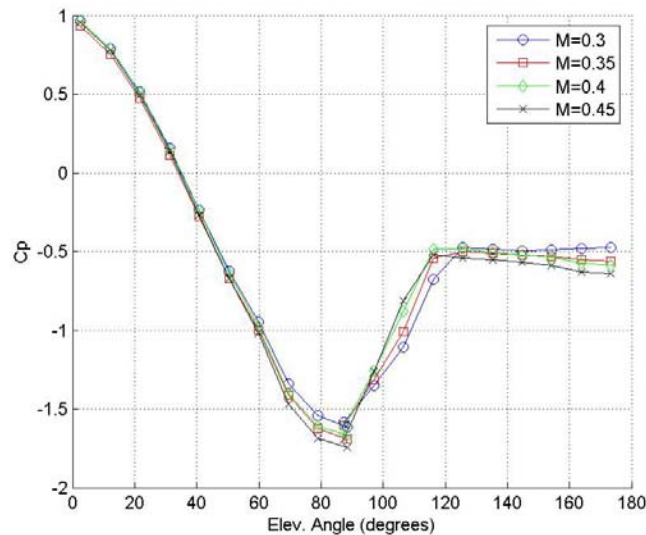
Figure 3. Normalized static pressures along the line of zero-degree azimuthal angle.

A. Steady pressure measurements

The hemispherical portion of the turret was equipped with a series of static pressure ports one inch apart. Results of normalized static-pressure measurements along the turret centerplane (at zero-degree azimuth angle) for different

elevation angles and Mach numbers are presented in Figure 3. An elevation angle of zero degrees corresponds to the upstream direction. Flow stagnates at the bottom of the hemispherical part of the turret (elevation angle of 0 degrees), accelerates along the front portion of the turret (elevation angles between 0 and 90 degrees), enters the region of an adverse pressure gradient on the back of the turret (elevation angles above 90 degrees) and eventually separates either after 120 degrees for lower Mach number of 0.3, or 115 degrees for higher Mach numbers of 0.35, 0.4 and 0.45. All normalized pressure data are collapsed on a single curve, indicating fully-developed flow around the turret.

B. Unsteady pressure measurements.

To characterize the temporal behavior of the wake behind the turret, 3 unsteady pressure sensors were placed in the wake. Sensor # 3 was placed on the mounting cylinder at azimuth angles of +135 degrees, 1.5" above of the mounting plate. Sensors # 5 and # 6 were placed downstream of the turret at the tunnel wall at locations shown in Figure 4.
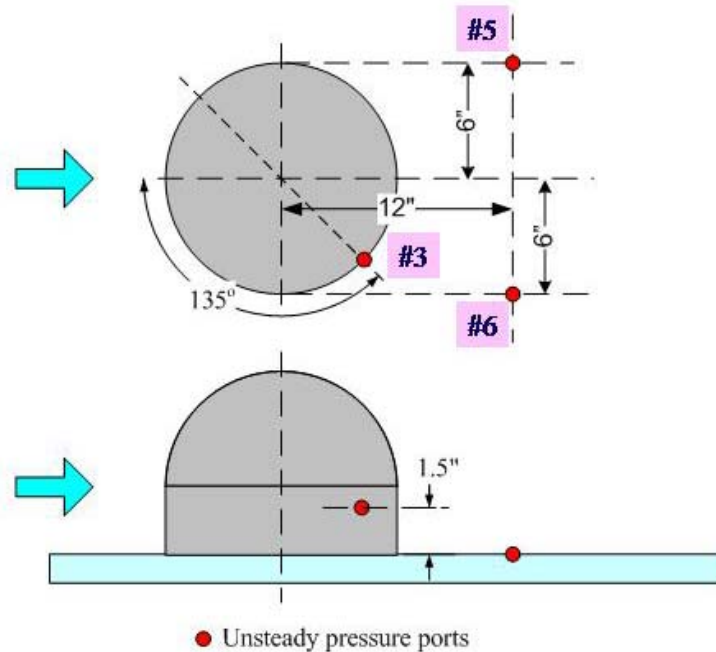

Figure 4. Locations of unsteady pressure sensors.

Unsteady-pressure power spectra for all three unsteady sensors at different Mach numbers are presented in Figure 5. Pressures in the wake behind the turret, Locations # 5 and # 6, exhibit a broad peak between 0.1 and 0.2 kHz, which increases in magnitude and shifts to higher frequencies with increasing Mach numbers. The turret-mounted sensor # 3 shows the presence of several small broad peaks on the surface of turret. The same data re-plotted for non-dimensional frequencies, $St_D = f D/U_{inf}$ are shown in Figure 6. The non-dimensional wake spectra show a single peak at $St_D = 0.35$, independent of Mach number, corresponding to the vortex shedding behind the turret, i.e., the wake vortices indicated in Figure 1. . Differences in pressure amplitudes can be contributed to a small asymmetry of the turret placement on the tunnel wall, see Figure 2, right plot.

III.   Optical Measurements

The turret is equipped with set of lenses and a mirror, which is designed to return a co-axial collimated beam back to the optical bench with minimal distortions; see Figure 7. The optical system consists of three elements: a positive lens, a negative lens, and a flat mirror. The positive lens is 6 inches in diameter (5 inch of clear aperture) with a leading radius of curvature of 6 inches, mounted flush with the turret surface. The negative lens is mounted on an adjustable platform and is designed to compensate for a spherical aberration from the positive lens. The collimated beam passing through the flow, positive and negative lenses, is reflected by the flat mirror back through the same region of the flow, thus increasing optical signal by a factor of two. The overall residual wavefront error of

the optical system is less than λ/8 (@ 633 nm) rms. Therefore, the optical system is equivalent to a flat mirror with a surface quality of λ/8.
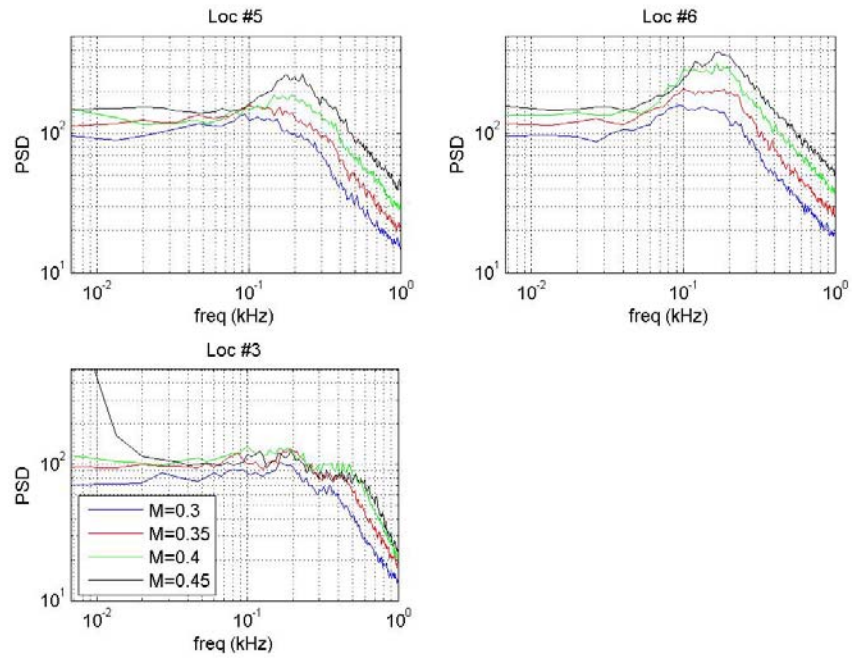

Figure 5. Unsteady pressure spectra for different sensors for several Mach numbers as a function of frequency.
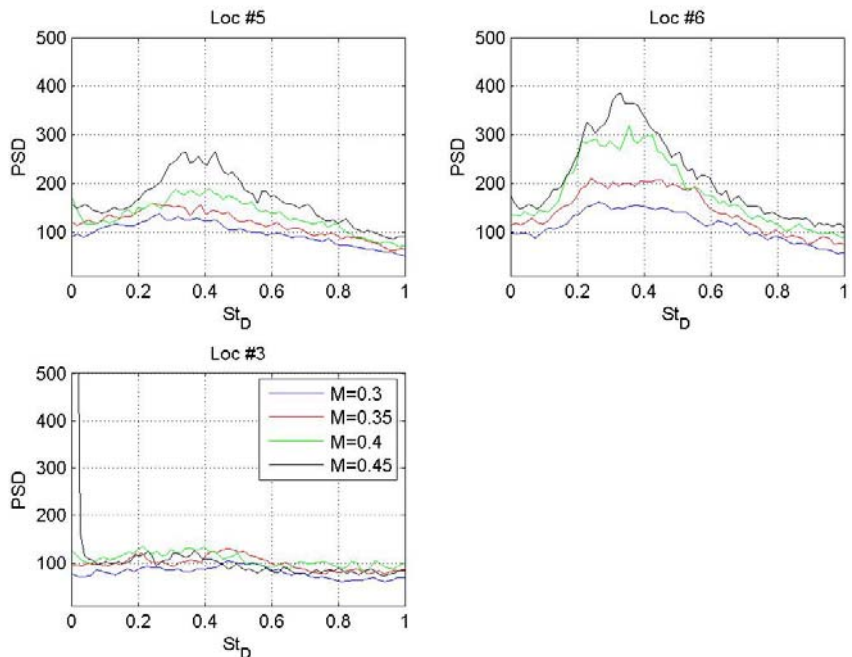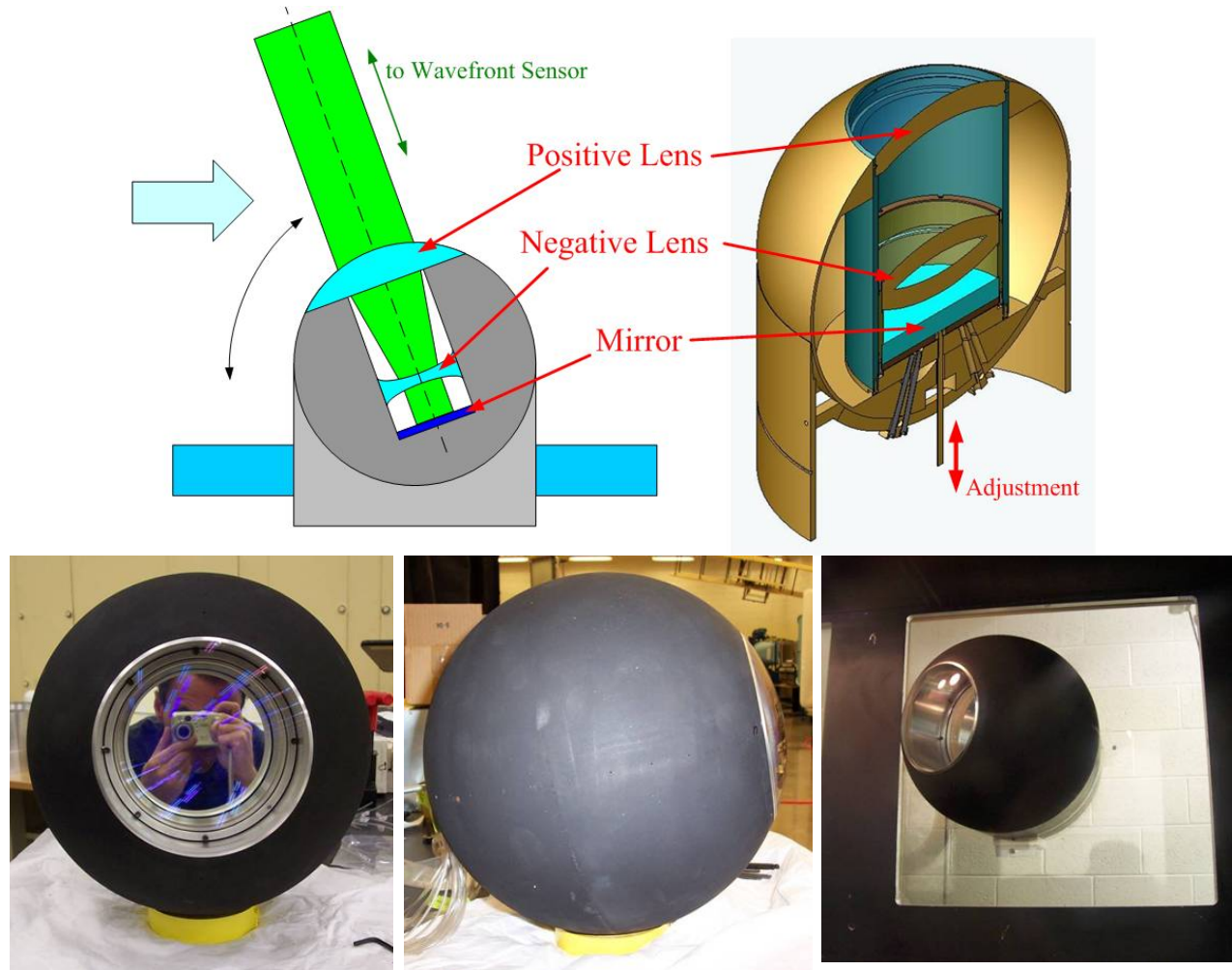

Figure 6. Unsteady pressure spectra for different sensors for several Mach numbers as a function of $St_D = f D/U_{inf}$**.**

Figure 7. Optical turret.

Three different optical wavefront devices, a Malley probe (Malley), a commercial 2-D wavefront sensor (WFs) and an 8x8 high-bandwidth wavefront sensor (8x8), were used to measure optical aberrations around the turret at a zero azimuthal angle at different elevation angles and Mach numbers.

C. Malley Probe results

The Malley probe principle of operation and data reduction procedure can be found in Refs 7-9. Here we briefly outline the essential details only. The Malley-probe optical set-up is shown in Figure 8. A small, 1mm diameter laser beam is split into two parallel laser beams spaced by 4 to 5 mm. Using two steering mirrors, the two beams are directed in and out of the optical turret section through an optically flat glass window mounted on the tunnel front wall. An optical turret reflects the beams coaxially along the same optical path back to the optical table, thus doubling the optical signal. The returning beams are separated from the incoming beams at the optical bench using a cube beam splitter and each beam is passed through a focusing lens onto Position Sensing Devices (PSD). The PSD measures each beam instantaneous deflection angles, which are digitally acquired with a 200 kHz sampling rate, sampling time of 10 seconds by a computer for post-processing analysis, outlined below,

Malley Probe Post-processing procedure.
1.   Measure streamwise deflections angles $\theta_1(t)$ and $\theta_2(t)$.
2.   Compute power density spectra for each deflection angle.
3.   Compute cross-correlation function $S(f)$, $S(f) = \left\langle \hat{\theta}_1^*(f)\hat{\theta}_2(f) \right\rangle - cross-spectral\ function$
4.   Remove vibration contamination by analyzing phase maps of Arg[S(f)]

5.   Calculate convective speeds U_c by calculating a time delay between two signals.
6.   Calculate 1-D wavefront slices OPD(t) assuming a Frozen Field hypothesis,

$$OPD(t) = -U_c \int \theta_1(t)dt$$

7.   Apply aperture, A_p, to OPD(t) results, remove instantaneous tilt component from each apertured slice and calculate residual OPD_{rms} for a given aperture.
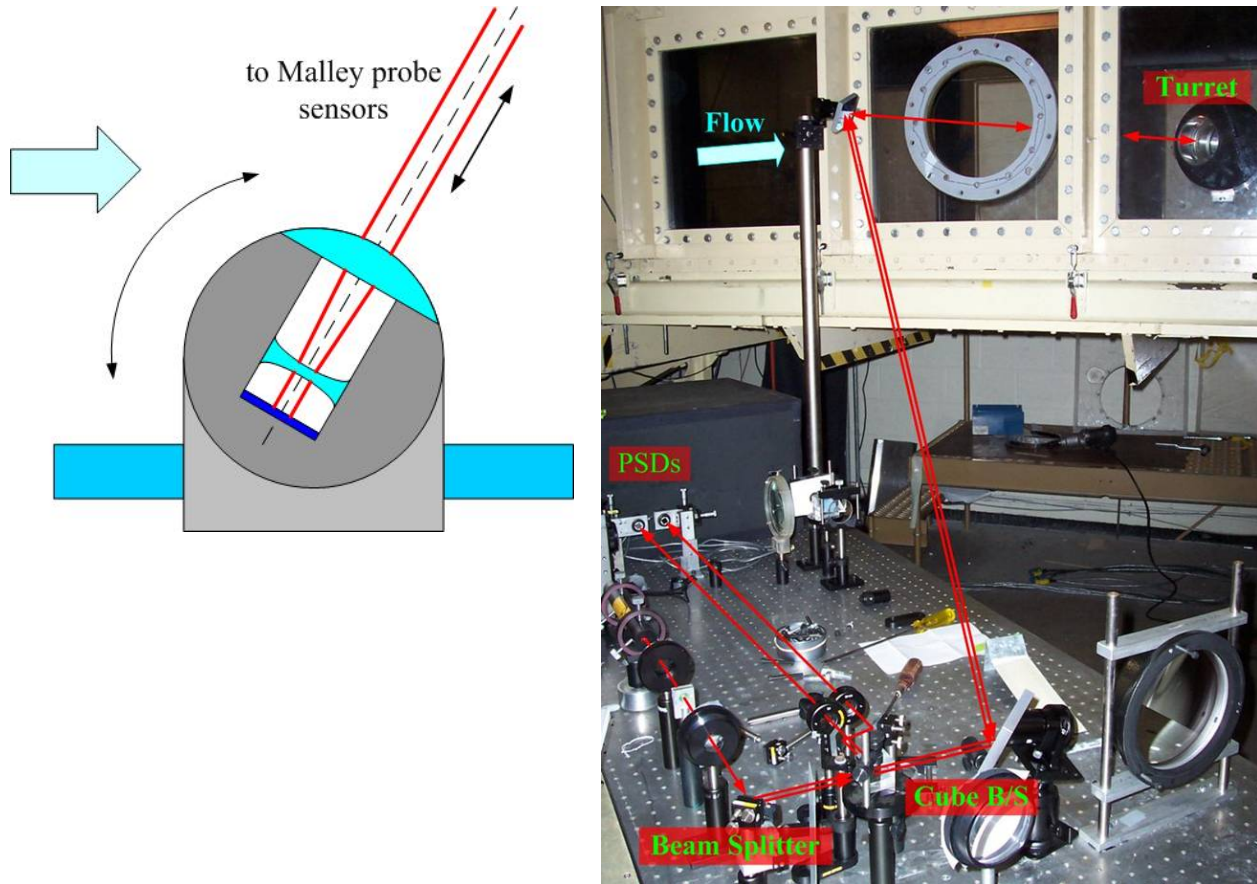
Figure 8. Malley probe schematic (left) and optical set-up (right).

Deflection angle power spectra plots for different elevation angles for M = 0.4 are presented in Figure 9. Spectra for all angles have strong low frequency, f < 0.7 kHz, components. For the back-looking angle of 132 degrees the laser beam passes through a shear layer formed in the separation region behind the turret, so the deflection angle spectrum have an additional, shear-layer related peak around 2 kHz. Narrow peaks in spectra are electronic noise.

Phase delay between two deflection-angle time series (phase plots) for different elevation angles at M = 0.4 are presented in Figure 10. All phase plots have a zero-phase correlation plateau at low frequencies below 0.8 kHz, upper center plot in Figure 10, suggesting the presence of stationary disturbances. The nature of these disturbances will be discussed later. All these stationary frequencies were removed using a low-pass filter before reconstructing 1-D slices of wavefronts. Above 0.8 kHz, the phase plots show a linear dependence with frequency. This indicates a convective nature of optically aberrating structures at high frequencies[8]. The presence of convective structures is evident for all elevation angles, even the forward looking angles, suggesting a complex flow structure around the turret.

Knowing the phase slope, the average time delay τ between the two Malley Probe beams can be found as Arg[S(f)]=$2\pi f\tau$, and for a given beam separation in the streamwise direction convective speeds of optically aberrating structures were calculated; results are presented in Figure 11. Flow accelerates over the front portion of the turret and decelerates on the back until it separates around 115 degrees. After this point, shear layer structures appear in the separation region with convective speeds of 0.8 of the freestream speed. These speeds are similar to shear layer convective speeds for the flat window turret, observed in Ref 5.
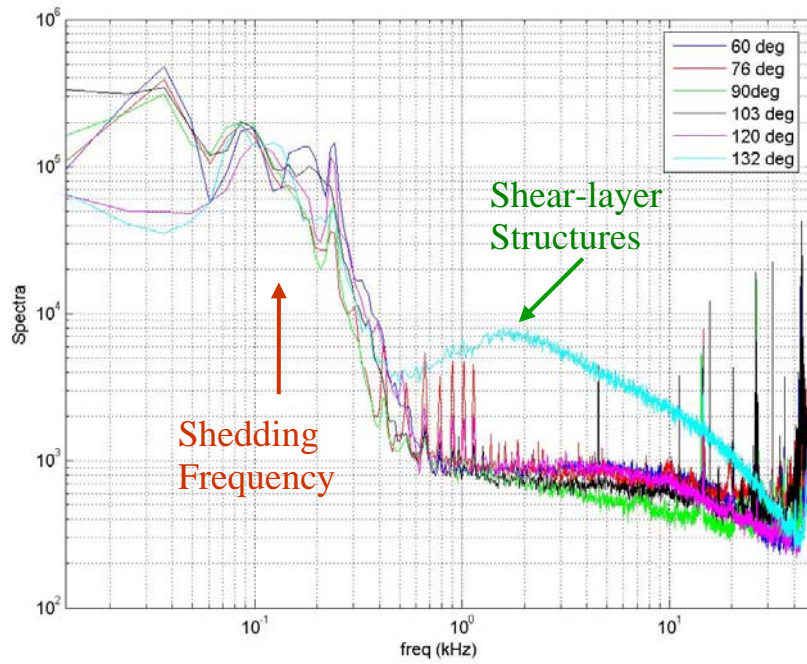
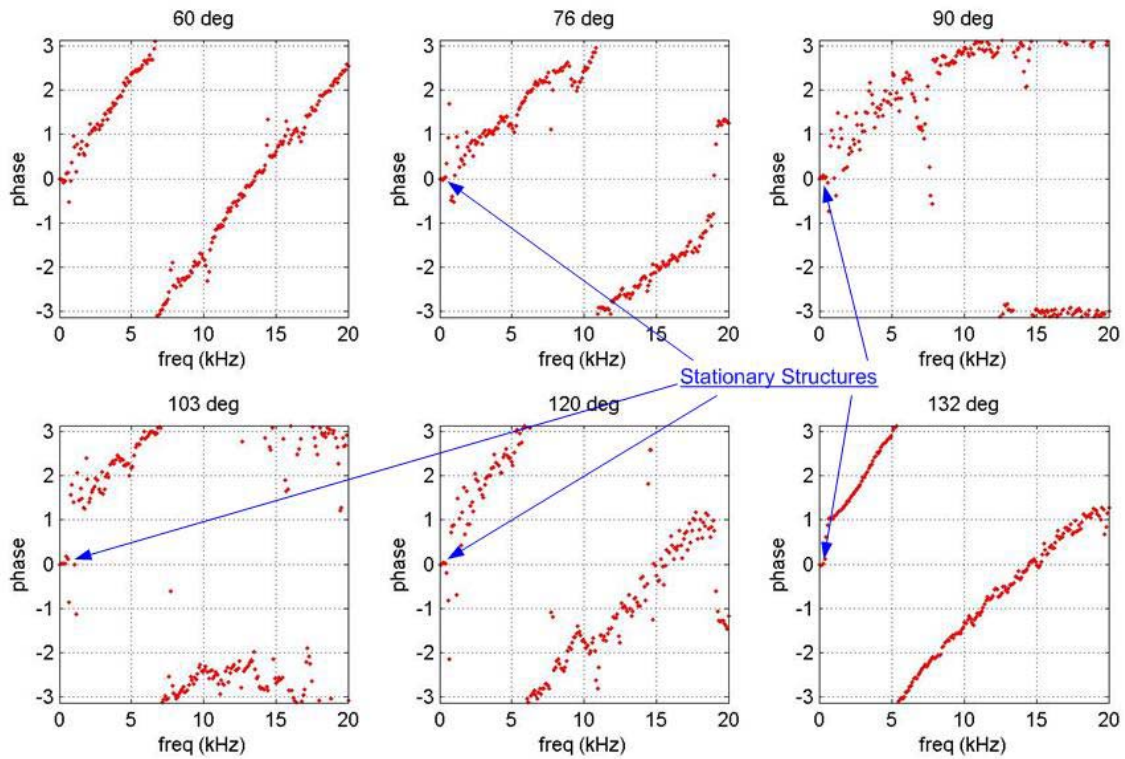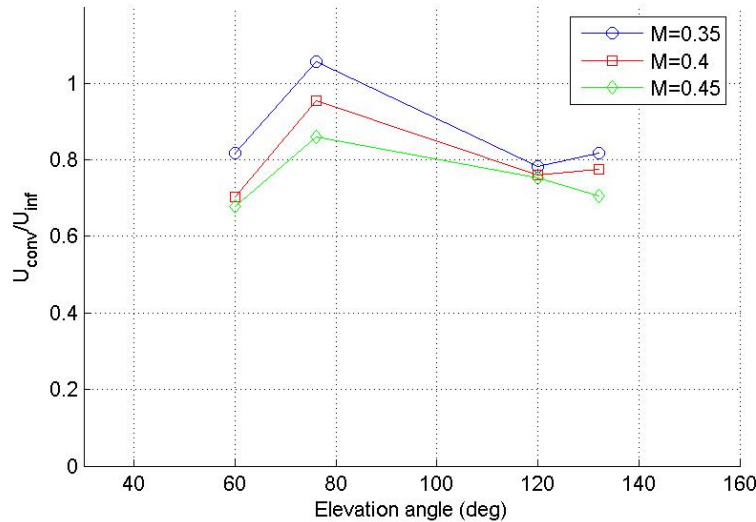**Figure 9. Deflection angle spectra for different elevation angles. M =0.4.**

Figure 10. Phase plots Arg[S(f)] for different elevation angles. M = 0.4.

Figure 11. Convective speeds of optical structures from Malley probe.

D. Wavefront sensor results

Uncorrelated 2-D wavefronts across the turret aperture were taken using a Wavefront Sciences CLAS-2D 2-dimensional wavefront system. A schematic and an annotated photograph of the optical set-up are presented in Figure 12. A frequency-doubled YAG:Nd laser with a pulse duration of 6 nsec was expanded to a 5-inch collimated beam and directed from the optical bench to the test section using two large mirrors. This beam was directed into the turret aperture radially and returned coaxially back to the bench. The return beam was then split using a cube beam splitter after being contracted to one-inch beam. The beam's optical distortions were measured using the 2-D Shack-Hartmann wavefront sensor with a 24 x 36 lenslet array. The wavefronts were sampled at 10 Hz. Two hundred wavefronts were recorded for each elevation angle and Mach number. Due to spherical aberrations imposed by the expanding optics, only a central, 4.5-inch-diameter portion was used to calculate wavefront error. Instantaneous tip/tilt was removed from each wavefront and an average aberration of the wavefront over the aperture was calculated as OPD_{rms}.

OPD_{rms} from the 2-D WaveFront sensor for different elevation angles at M = 0.4 are presented in Figure 13. Also shown for comparison are results for OPD_{rms} from the Malley probe apertured to a 4.5" beam. Malley probe and WF results give similar numbers for elevation angles above 120 degrees. In this region, the dominant aberrations are the moving shear-layer structures. WF results are consistently higher than the Malley data for all angles below 100 degrees. The reason of this discrepancy is that all zero-phase correlations, i.e. below 800 Hz, were filtered out from Malley probe data during the post-process analysis using a digital filter. Thus, any physical stationary aberrations were removed from resulting optical distortions from the Malley probe data.

To investigate the nature of stationary aberrations at forward looking angles, selected wavefronts for elevation angles of 76, 90 and 132 degrees at M = 0.4 are presented in Figure 14. Small to moderate deviations (≤ 0.12 um) from a planar wavefront can be observed on both sides of the aperture for 76 and 90 degrees cases. These aberrations we hypothesize may be due to the presence and unsteady motion of the necklace vortex formed at the bottom front portion of the turret referred to earlier. These necklace-vortex low-frequency motions modify the potential flow around the turret and create unsteady but *stationary* distortions on the laser beam. These aberrations are removed from Malley probe data, which results in underpredicting optical aberrations using the Malley probe at forward looking angles, as in Figure 13.

After the flow separates at 115 degrees, spanwise shear-layer structures appear downstream of the separation location (c.f. below). These are clearly visible for the 132 degrees case in Figure 14. Although the flow separates at 115 degrees for M = 0.4, shear layer structures are developed some distance downstream of the separation point. Averaged amplitudes of wavefronts over the aperture for 120 and 132 degrees cases for M = 0.4 are presented in Figure 15. For the 120 degree case, the OPD_{rms} is uniformly distributed over the aperture with levels of 0.04 microns. At 132 degrees, the OPD_{rms} is around 0.04 microns for the front half of the aperture and increases downstream starting from the middle of aperture. This marks the onset of shear-layer structure formation. A linear

growth of the shear layer leads to an observed linear increase in wavefront amplitudes at the downstream half of the aperture.
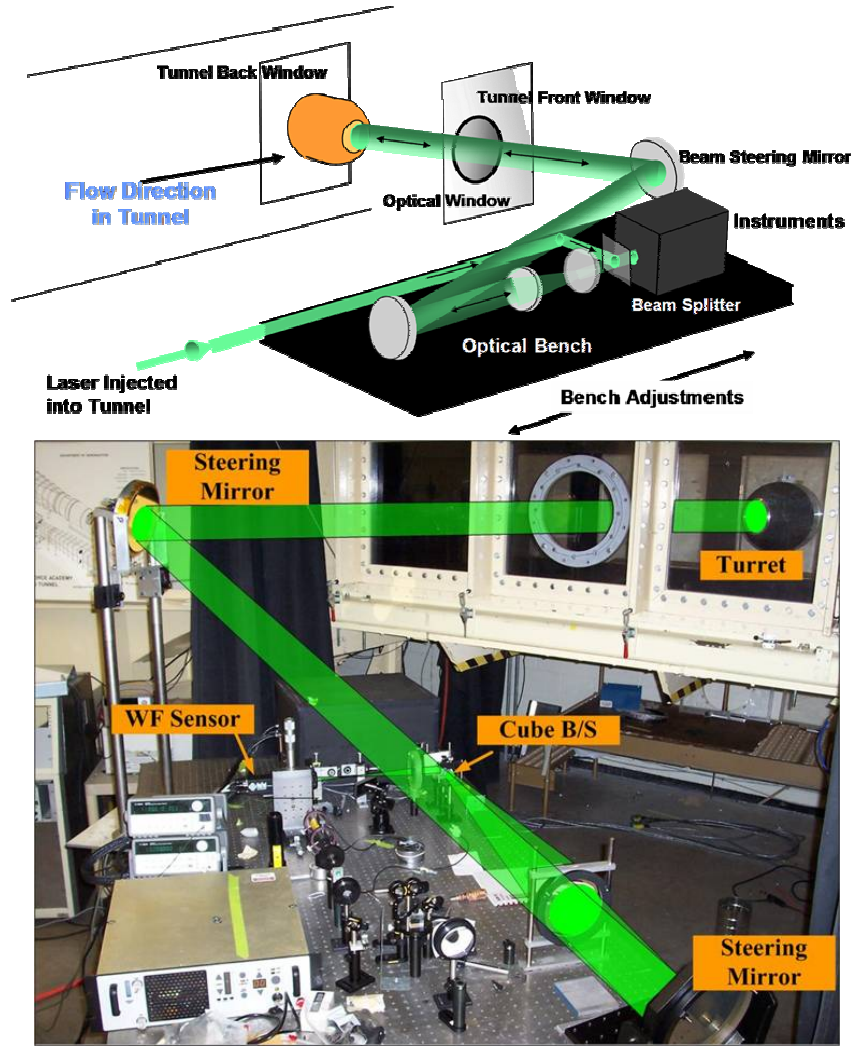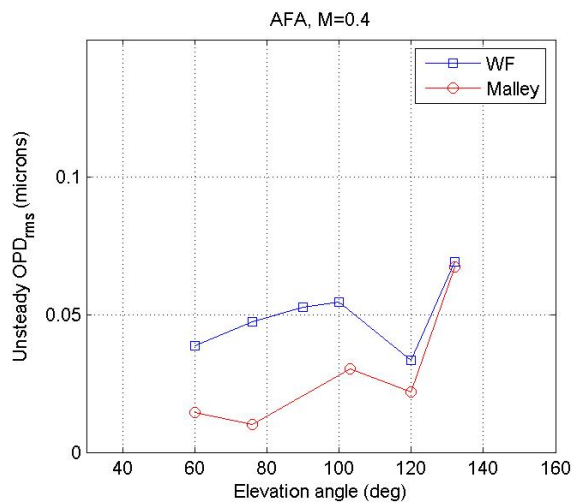

Figure 12. 2-D Wavefront Set-Up.

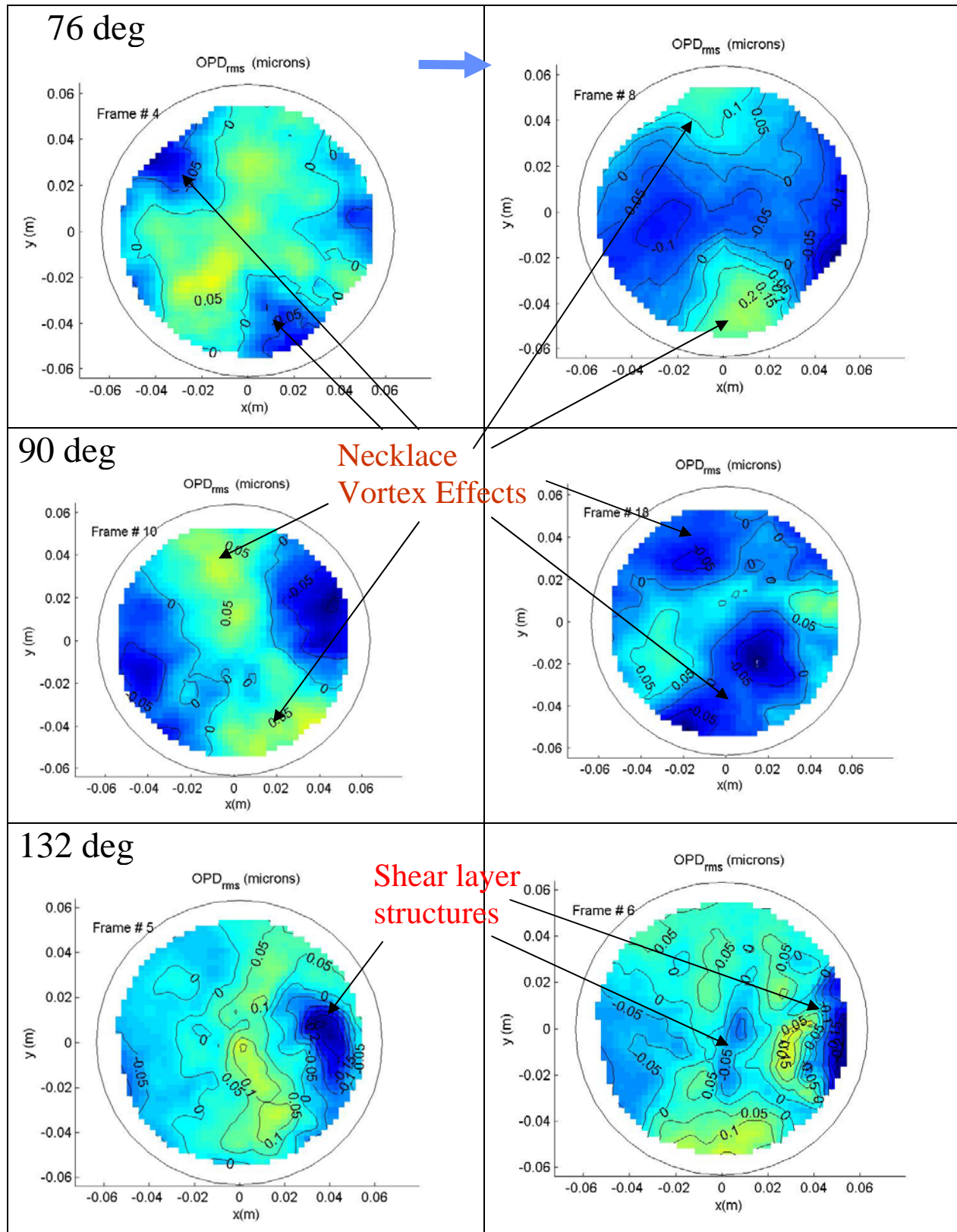**Figure 13. OPDrms from WaveFront and Malley probe measurements.**

Figure 14. Selected wavefronts for 76, 90 and 90 degrees. M = 0.4. Flow goes from left to right.
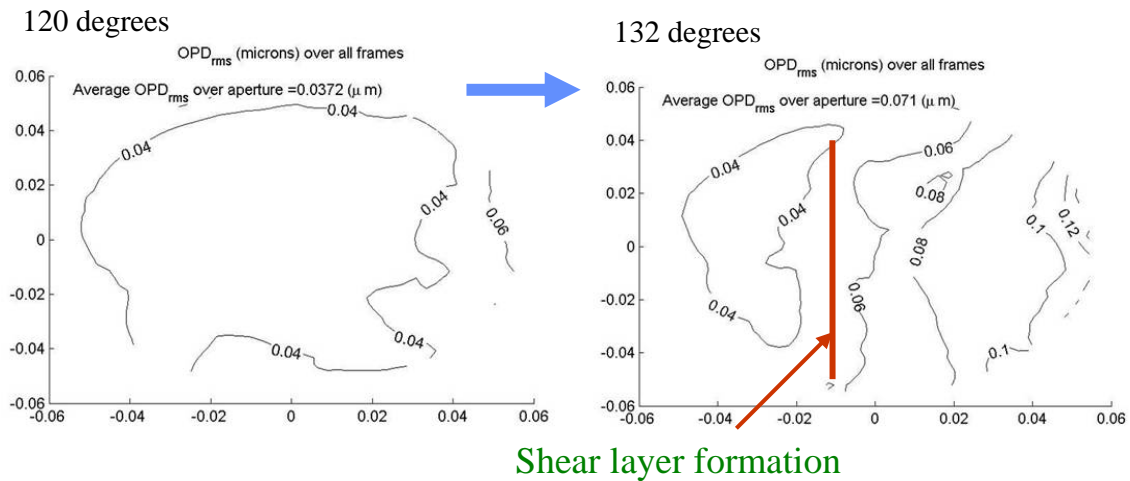
120 degrees

132 degrees

Shear layer formation

Figure 15. Wavefront variations over the aperture for back-looking elevation angles. M = 0.4.

E. 8 x 8 High-Bandwidth Wavefront Sensor Results.

A high-bandwidth wavefront sensor was also used to measure the temporal-spatial evolution of wavefronts. The 8x8 sub-aperture, high-bandwidth wavefront sensor is a further development of the 4x4 sub-apertures high-bandwidth wavefront sensor jointly developed with Oceanit[10]. It is a Hartmann-type wavefront sensor with a 80 mm x 80mm 8 x 8 lenslet array (Figure 16, left) and an 8 x 8 square array of analog position sensing devices to measure beam centroids, (Figure 16, right). The analog nature of the data acquisition board allows wavefront sampling rates in access of 100 kHz; however a sampling rate of 78 kHz was used in this series.

8x8 Lenslet Array   8x8 Sensor Board
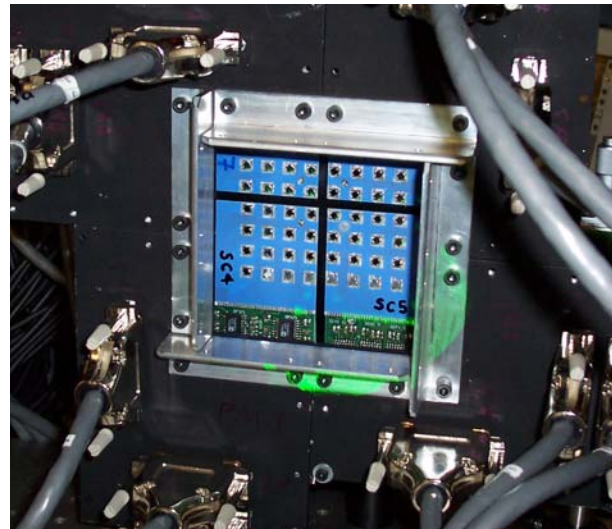

Figure 16. 8 x 8 Wavefront sensor.

The high-bandwidth wavefront sensor optical set-up is shown in Figure 17. A continuous wave frequency-doubled YAG:Nd laser beam was expanded to 5", as was done for the Wavefront Sciences WFS, and transmitted through the flow to the turret. The reflected beam was returned coaxially to the bench and again split after contraction to one-inch, then re-expanded onto the 8 x 8 wavefront sensor using a cube beam splitter. Only the middle portion of the returned beam with a diameter of 3" (not 4.5 ") was used to reconstruct wavefronts as follows:
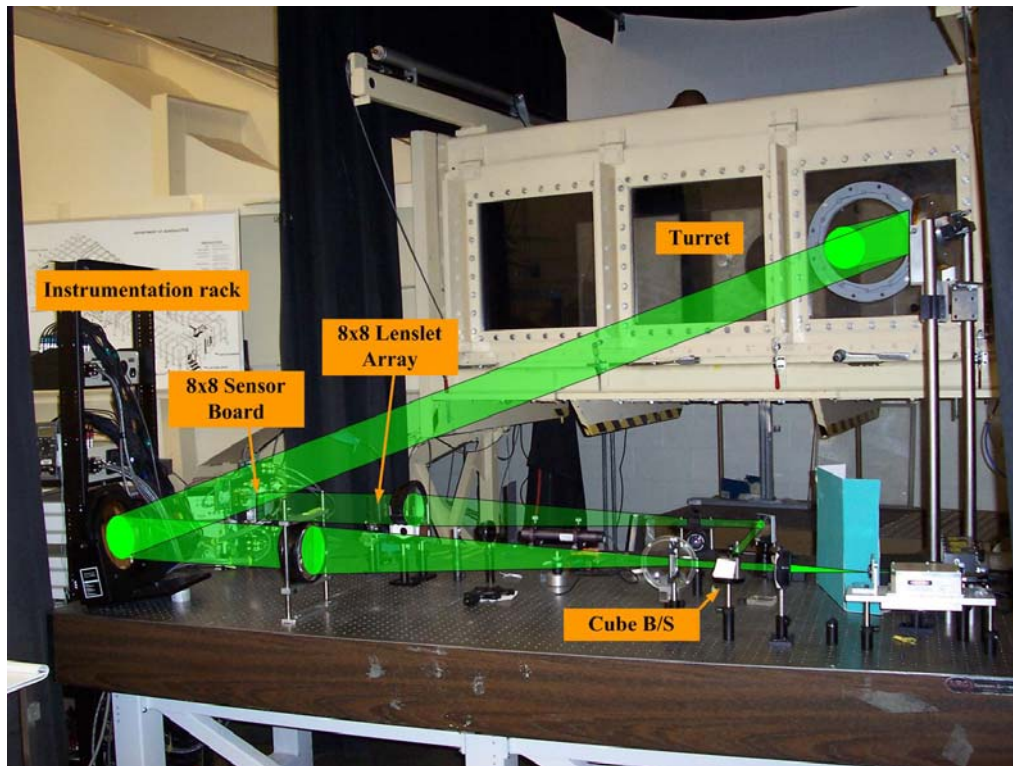
Figure 17. 8 x8 wavefront sensor optical set-up.

8x8 sensor data reconstruction procedure
1. 128 channels (2 channels per each sensor) are sampled at 78 kHz for 10 seconds.
2. Using calibration constants, signals are converted to deflection angles $\theta(t)$.
3. Deflection angles' time histories are filtered using either a low- or high-pass filter to separate stationary and traveling structures.
4. Wavefronts are computed from deflection angles, $WF(t) = grad(\theta)$.
5. Piston and Tip/Tilt modes are removed from each wavefront.
6. Steady wavefront is computed over all wavefronts.
7. Steady component is removed from each wavefront.
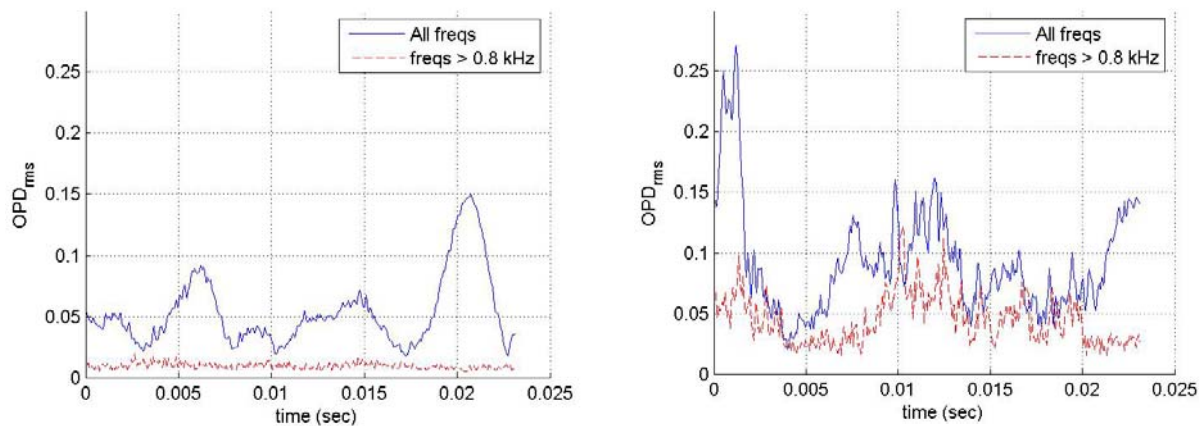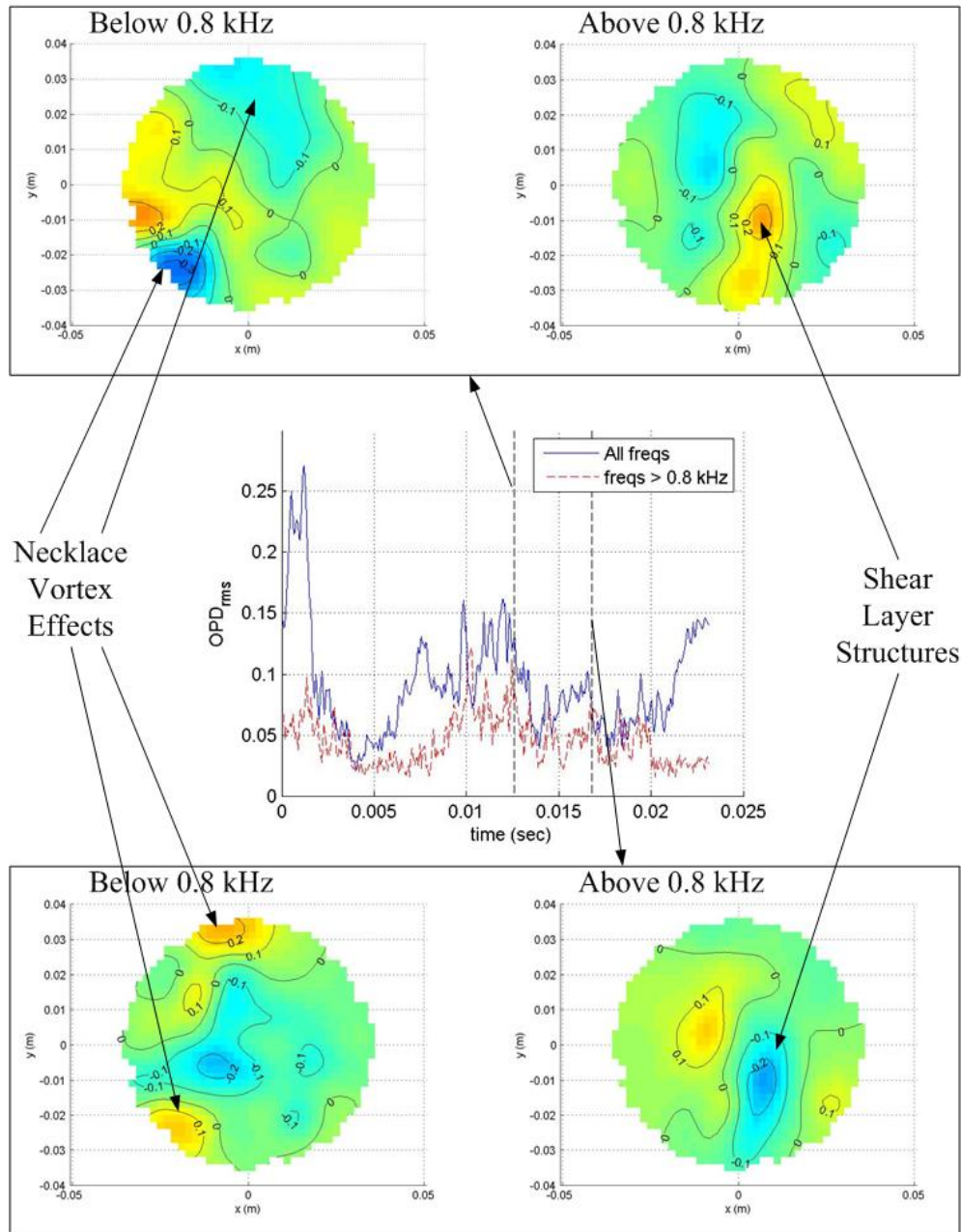8. Resulting wavefronts reflect *unsteady* components only.

Figure 18. Temporal evolution of OPD$_{rms}$ from 8x8 sensor for 120 degree (left) and 132 degree (right) cases. M = 0.4.

Figure 19. Reconstructed wavefronts for low (below 0.8 kHz) and high (above 0.8 kHz) frequencies from 8x8 high-bandwidth WF sensor.

By filtering the wavefront gradients using the low-pass filter, wavefronts could be reconstructed that contain only the stationary aberrations, and by filtering the gradients with a high-pass filter wavefronts could be reconstructed that contain only the convecting distortions. The temporal evolution of the OPD_{rms} over the aperture at M = 0.4 are presented in Figure 18. Both high-pass (above 0.8 kHz) filtered and no-filtered cases for two angles of 120 and 132 degrees are shown. For the 120 degree case, most of optical aberrations are located at low frequencies, below 0.8 kHz. These exhibit large amplitude, low frequency deviations. This is due to the slow unsteady variations we have attributed to the unsteadiness of the necklace vortex around the turret base. High frequencies, above 0.8 kHz, are responsible only for a small portion of optical aberrations for this angle. However, for the 132 degree case, the high, shear-layer-related frequencies cause most of optical aberrations. Low, necklace-vortex related frequencies occasionally influence optical distortions.

As discussed above, based on the Malley probe data we expect that the unsteady but stationary necklace-vortex effects and its association with its entrainment into the unsteady turret wake are the main cause of optical aberrations for frequencies below 0.8 kHz; moving shear-layer structures dominate optical distortions for all frequencies above 0.8 kHz. Further understanding of these low- and high-pass filtered wavefronts can be gained by examining selected wavefronts as in Figure 19; for two time instances marked by dashed lines on the middle plot, low- and high-frequency components of the wavefront are shown. Flow goes from left to right. For the low-frequency part of the wavefront, necklace-vortex effects are clearly present on both sides of the aperture. The high-frequency component of the wavefront reveals shear layer structures convecting across the aperture. Compared with the high spatially resolved wavefront measurements at 132 degrees using the Wavefront Sciences wavefront sensor, Figure 14, 8x8 sub-apertures are sufficient to resolve the main components of shear-layer structures, but fine details are obviously missing. Therefore, the high temporal resolution and analog nature of the output signal allows isolating and inspecting wavefront components at different frequency bands and separating stationary structures, like necklace-vortex effects from convective aberrations, like the shear layer structures. A high-spatial-resolution 2-D wavefront sensor having hundreds of subapertures, cannot currently separate stationary and moving components of the optical wavefront directly. Thus, the 8x8 high-bandwidth sensor combines high temporal resolution and an analog nature of the output signal, typical for the Malley probe, and a decent spatial resolution, like a conventional 2-D wavefront sensor. This ability of the 8x8 sensor to reconstruct corresponding wavefronts for different frequency bands has now proven to be able to provide valuable information about the flow that is invaluable to adaptive-optic analysis and design, not available by other means.
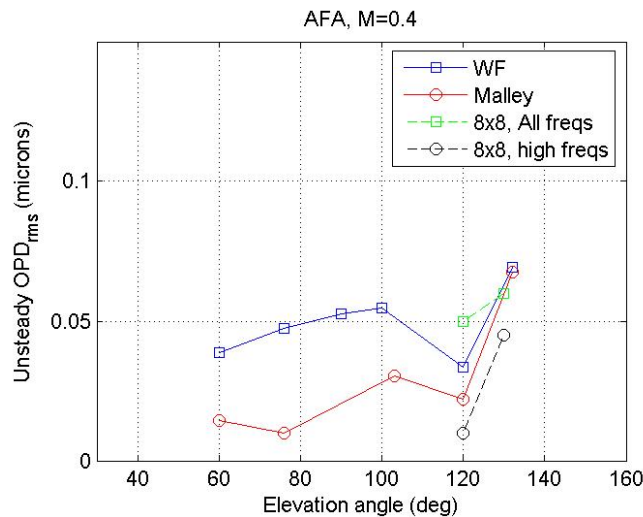

Figure 20. OPD$_{rms}$ for different elevation angles for all measurement devices.

A summary of the time-averaged optical measurements using all three sensors are presented in Figure 20. Unfiltered 8x8 sensor data (3" aperture) at elevation angles of 120 and 132 degrees are similar to WF results (4.5" aperture), and give about 0.05 microns of optical aberrations at M = 0.4. High-pass filtered 8x8 sensor results are similar to the Malley probe data (4.5" aperture), since neither of them include stationary effects of the necklace vortex. Overall, optical aberrations are high for backward looking angles, where structures in the separated shear layer play a dominant role.

IV.   Flow Visualization Results

Surface flow visualization was accomplished with a 1:2 mixture of rubbing alcohol (95% isopropyl alcohol) and Aeroshell Oil 100. This oil was chosen because it contains a fluorescent detergent visible under black light, and readily highlights flow patterns. The mixture was hand-sprayed from a squeeze bottle onto the sphere and wall region in the vicinity of the hemisphere, approximately 30 cm upstream and 100 cm downstream of the turret. This allowed visualization of body surface flow as well as upstream turning and wake behavior. Once the mixture was applied, the tunnel was brought up to speed for and held constant for 5 to ten minutes. This allowed the mixture to mark the flow, and a substantial amount of the alcohol to evaporate, stabilizing the patterns. As quickly as possible, the tunnel was shut down and opened, the black light shone on the wall and photos taken before gravitational effects altered the flow lines. Cleaners were then applied to the wall to remove the oil before a new run was initiated. Figure 21 shows the patterns under normal and black light.
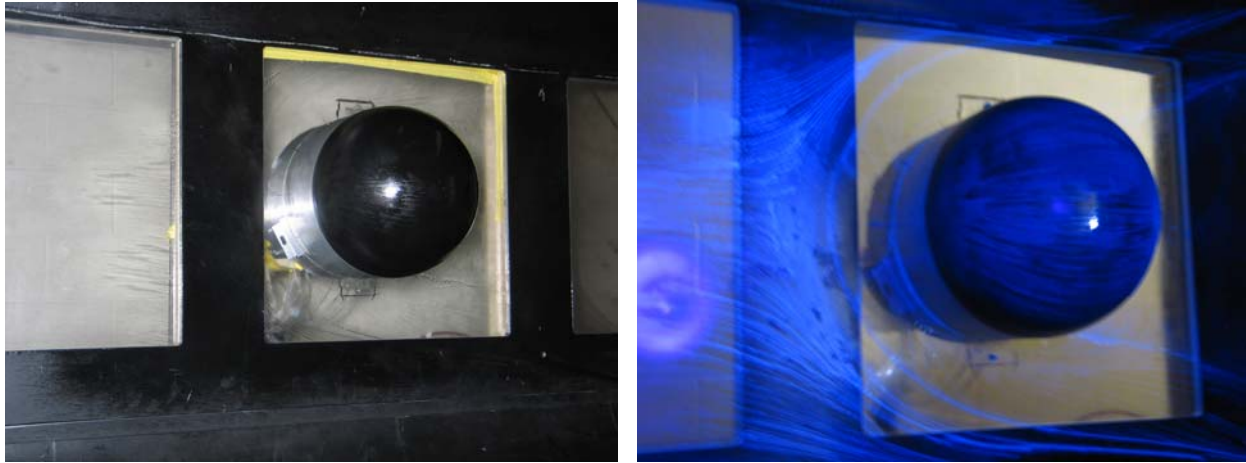
Figure 21. Typical view of flow patterns under normal and black light.

Results of the oil surface-flow visualization for different Mach numbers are presented in Figure 22. Both the necklace vortex and the wake behind the turret have a complex topological structure. For example, the necklace vortex has two negative attractor lines nested between three positive attractors, which suggest a nested vortical structure inside of the necklace vortex. The wake behind the cylinder reveals the presence of the circulation bubble behind the turret, as streamlines travel upstream of the flow in this region. Flow on the downstream half of the turret also reveals a complex vortical structure, which weakly depends on Mach number, as can be observed by comparing flow topologies on the turret for different Mach numbers in Figure 22. This complex wake structure behind the turret will definitely impose large levels of optical aberrations on the laser beam passing through the wake region.

V.   Conclusions

This paper compliments an earlier paper[5] that examined a similar turret but with a flat window. In the present study the flat window was replaced with a conformal window. This seemingly minor change in the turret from an optical point of view greatly modified the environment from that of the flat-windowed turret in the aft quadrant of the turret. Whereas in the flat-windowed case the flow separation was fixed by the surface-slope discontinuity, in the conformal case the separation line becomes unsteady and Mach number dependent. On the positive side, the conformal window extends the useful filed of regard to approximately 120 degrees. On the negative side, the added complexity of the conformal-window flow makes for a more-unpredictable optical environment.

This paper also underscores the importance of using a suite of optical instruments to access the optical environment around turrets. The use of the Malley Probe allowed for highly spatially- and temporally-resolved 1-D slices of OPD data for the highest-frequency convecting aberrations in the flow. The untime-resoled but high-spatial detail of the convectional 2-D wavefronts provided information about the importance of small-scale aberrations in the flow, but could not provide a rational for the differences between Malley-Probe data and 2-D wavefronts for elevation angles less than 120 degrees. The high-bandwidth 8x8 2-D wavefront sensor through analysis technique developed during this study was able to explain these differences and add greatly to our understanding of the complex flow physics creating the optical environment. Finally, the pressure and flow-visualization data added confidence to our understanding we have given here.

M =0.3   M=0.3

M = 0.35, M = 0.4
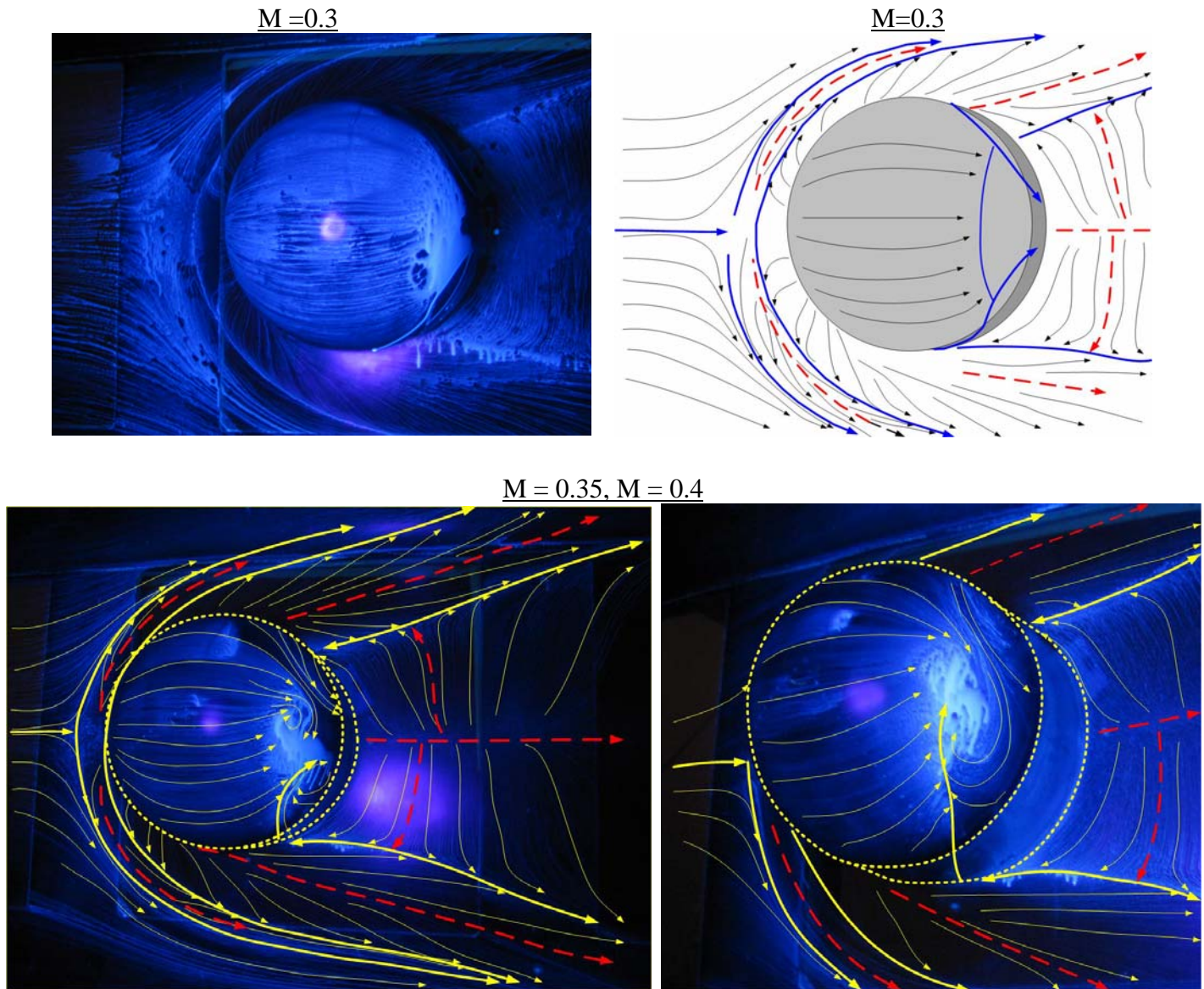
Figure 22. Surface flow topology on and around the turret: flow visualization (right) and schematic of surface streamlines (thin solid lines), stable (thick solid lines) and unstable (thick dashed lines) manifolds for different Mach numbers. Turret contour is outlined by a dotted line.

Acknowledgments

References

[1]Gilbert, K.G., "Overview of Aero-Optics," Aero-Optical Phenomena, Eds. K.G. Gilbert and L.J. Otten, Vol. 80, Progress in Astronautics and Aeronautics, AIAA, New York, 1982, pp. 1-9.

[2]Jumper, E.J. and Fitzgerald, E.J., "Recent Advances in Aero-Optics," *Progress in Aerospace Sciences*, Vol. 37, 2001, pp. 299-339.

[3]Fitzgerald, E.J. and Jumper E.J., "The Optical Distortion Mechanism in a Nearly Incompressible Free Shear Layer," *Journal of Fluid Mechanics*, Vol. 512, 2004, pp. 153-189.

[4]Kyrazis, D., "Optical degradation by turbulent free shear layers," *SPIE*, Vol. 2005, 1993.

[5]S. Gordeyev, T. Hayden and E. Jumper, "Aero-Optical and Hot-Wire Measurements of the Flow Around the Hemispherical Turret With a Flat Window", 35th AIAA Plasmadynamics and Laser Conference, Portland, Oregon, 28 Jun - 1 Jul, 2004, AIAA Paper 2004-2450.

[6]S. Gordeyev, E. Jumper, T. Ng and A. Cain, "The Optical Environment of a Cylindrical Turret with a Flat Window and the Impact of Passive Control Devices", 36th AIAA Plasmadynamics and Laser Conference, Toronto, Canada, 6-9 June, 2005, AIAA Paper 2005-4657.

[7]Malley, M., Sutton, G.W., and Kincheloe, N., "Beam-Jitter Measurements for Turbulent Aero-Optical Path Differences", *Applied Optics*, **31**, 1992, pp. 4440-4443.

[8]S. Gordeyev, E. Jumper, T. Ng and A. Cain, "Aero-Optical Characteristics of Compressible, Subsonic Turbulent Boundary Layer", 34th AIAA Plasmadynamics and Lasers Conference, Orlando, Florida, 23-26 June, 2003, AIAA Paper 2003-3606.

[9]D. Duffin, S. Gordeyev and E. Jumper, "Comparison of Wavefront Measurement Techniques on a Two-Dimensional Heated Jet", 35th AIAA Plasmadynamics and Laser Conference, Portland, Oregon, 28 Jun - 1 Jul, 2004, AIAA Paper 2004-2446.

[10]S. Gordeyev, D. Duffin and E. Jumper, "Aero-Optical Measurements Using Malley Probe and High-Bandwidth 2-D Wavefront Sensor", International Conference on Advanced Optical Diagnostics in Fluids, Solids and Combustion, Tokyo, Japan, 4-6 Dec, 2004.